Effect of the Electrical Energy Conversion on Optimal Cycles for Pumping Airborne Wind Energy

Jeroen Stuyts, *Student Member, IEEE*, Greg Horn, Wouter Vandermeulen, Johan Driesen, *Senior Member, IEEE*, and Moritz Diehl, *Member, IEEE*

***Abstract*—Airborne wind energy harvesting offers an alternative to traditional wind turbines by flying crosswind cycles with a tethered airfoil. By reeling in and out the tether periodically, net electrical power can be generated. When looking for the optimal cycle to fly, one should optimize for maximal electrical power generation. However, the conversion from mechanical to electrical power was not yet included in the models. In this paper, it is shown that by including an electrical energy conversion model into cycle optimization, the electrical output of the system increases and the acquired system can be used in a broader range of wind speeds. The approach is illustrated with experimentally verified models.**

***Index Terms*—Airborne wind energy (AWE), drives, energy conversion, optimal control, wind energy, wind power generation.**

I. Introduction

RENEWABLE power generation is gaining lots of attention. Three techniques, in particular, are widely accepted and being used: wind turbines, solar panels, and hydropower. There is, however, still a strong interest in finding new ways to harvest renewable energy. One of those ways is airborne wind energy (AWE). As theoretical wind power extraction is proportional to the wind velocity cubed [1] and wind velocity gets higher as altitude increases, it is advantageous to get as high as possible. AWE addresses this by using an airfoil which is connected to the ground only by a tether. Generators can then be onboard the airfoil, or on the ground, driven by periodic length variations of the tether, as shown in Fig. 1.

Manuscript received December 10, 2013; revised March 10, 2014 and June 05, 2014; accepted August 12, 2014. Date of publication September 16, 2014; date of current version December 12, 2014. This work was supported in part by Research Council KUL: PFV/10/002 Optimization in Engineering Center OPTEC, GOA/10/09 MaNet, and GOA/10/11 Global real-time optimal control of autonomous robots and mechatronic systems; in part by Flemish Government: IOF/KP/SCORES4CHEM, FWO: Ph.D./postdoc grants and projects: G.0320.08 (convex MPC), G.0377.09 (Mechatronics MPC); in part by IWT: Ph.D. Grants, projects: SBO LeCoPro; in part by Belgian Federal Science Policy Office: IUAP P7 (DYSCO, Dynamical systems, control and optimization, 2012-2017); and in part by EU: FP7-EMBOCON (ICT-248940), FP7-SADCO (MC ITN-264735), ERC ST HIGHWIND (259 166), Eurostars SMART, ACCM. Paper no. TSTE-00522-2013.

J. Stuyts, W. Vandermeulen, and J. Driesen are with the Department of Electrical Engineering, ESAT-ELECTA, KU Leuven, 3001 Heverlee, Belgium (e-mail: jeroen.stuyts@esat.kuleuven.be).

G. Horn is with the Department of Electrical Engineering, ESAT-STADIUS, KU Leuven, 3001 Heverlee, Belgium (e-mail: greghorn@esat.kuleuven.be).

M. Diehl is with the Department of Electrical Engineering, ESAT-STADIUS, KU Leuven, 3001 Heverlee, Belgium, and also with the Department of Microsystems Engineering, IMTEK, University of Freiburg, 79110 Freiburg, Germany.

Digital Object Identifier 10.1109/TSTE.2014.2349071

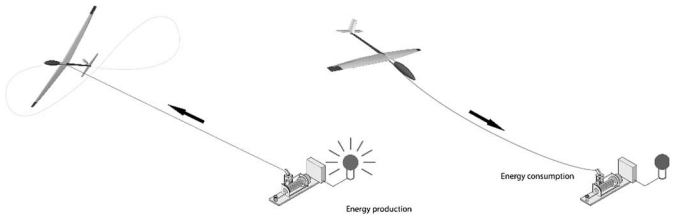


Fig. 1. Example of a pumping cycle with a reel-in and a reel-out phase as achieved by Ampyx Power [12].

To validate and test the concept, a test setup is required, which needs various electrical components. In the past, a scaled indoors carousel has been built at KU Leuven [2]; however, more extensive testing is required, and therefore, an outdoors carousel had to be built as well. The mechanical and electrical designs were developed in two master's theses at KU Leuven [3], [4], and the setup is currently built as part of the ERC project HIGHWIND. The tests and drive used throughout this paper are further described in [4].

To find the cycle which maximizes the harvested energy, numerical trajectory optimization techniques have been used in the past [5]–[10]. So far, the goal was to find the optimal mechanical energy-generating cycle. Since the goal is to generate electricity, an important aspect had not been integrated: the conversion from mechanical energy to electrical energy using a drive, i.e., a system with an electrical motor/generator and converters. An electrical energy conversion system has been modeled and integrated before [11]. However, the focus here lay on the grid integration and not on the interactions between the electrical conversion system and the mechanical system, nor the effect of the electrical conversion system on the optimized cycles.

The integration of this drive into the optimization is done in two levels: adding drive constraints to achieve a physically achievable cycle and adding drive efficiency to achieve the real electrical output power, instead of the mechanical output power. A couple of cases are then created by optimizing for maximal generated mechanical energy and for maximal generated electrical energy, and doing so, with and without constraints.

This enables us to look at the mechanical output power (the optimum if the drive was 100% efficient) and compares this to the electrical power (which is the real output). It is shown that optimizing electrically yields better real-world results and that it enables the drive to be used in a broader range of wind speeds.

1949-3029 © 2014 IEEE. Personal use is permitted, but republication/redistribution requires IEEE permission.
See http://www.ieee.org/publications_standards/publications/rights/index.html for more information.



Fig. 2. Ground station of Highwind: the carousel, without kite.

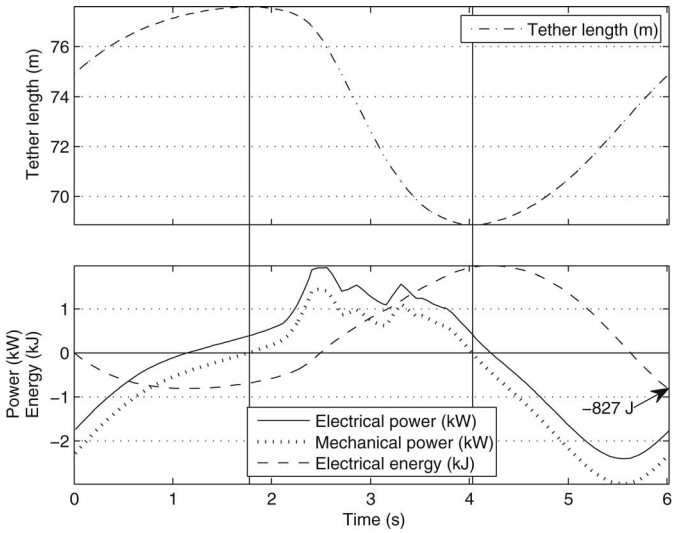


Fig. 3. Electrically optimized constrained pumping cycle at 5.5 m/s, showing tether length, electrical and mechanical power, and harvested energy versus time.

Both drive constraints and drive efficiency are based on a real system and experiments thereof. Their physical parameters were then integrated into the optimization tool. The results of optimizations presented in this paper are thus simulation results using the real physical parameters.

This paper is organized as follows: First, the experimental AWE setup is described, then the methodology is explained for including the electrical energy conversion in the optimization, next the optimization itself is explained, and finally, the optimization results are discussed.

II. Experimental AWE Setup

The outdoors carousel is an experimental setup required for extensive testing of all the software and procedures. The mechanical design is based on the indoors carousel [2], and it was obvious that also for this improved design, a new electrical design was required.

Fig. 2 shows the practical realization. As can be seen, the carousel is mounted on a trailer to enable outdoors use and to make it practical to move around.

The idea of the HIGHWIND project is to use a rigid-wing kite on a tether to fly crosswind loops downwind in order to harvest wind energy as described in [13]. When flying high-speed loops, the crosswind trajectory enables high lift for the kite and thus high tension on the tether. As the tether reels out during this phase, electricity can be generated in an electrical generator driven by a drum on which the tether is wound. At a certain point, the kite is reeled in at low tether tension, using less energy than it has previously generated. When repeating this pattern, wind energy is being harvested. Such a cycle is called a pumping cycle and is depicted in Fig. 1.

Fig. 3 shows a typical power-generating trajectory. The tether length is shown over time in order to see when the system is generating (negative power) and consuming power (positive power). The two vertical lines are added to mark the start of the reel-in and reel-out phase. It can be seen that when the kite starts reeling in (tether length gets shorter), the mechanical power becomes positive. When the kite starts reeling out (tether length gets longer), the mechanical power becomes negative. Due to the loss in the drive, the electrical power will always lie above the mechanical power, either consuming more or generating less power. The electrical energy is the integral of the electrical power and thus shows how much energy is being generated. As can be seen, at the end of one cycle, electrical energy is generated (827 J).

III. Methodology

A. Drive System

The selected motor is an 8.2 kW Siemens Simotics Permanent Magnet Synchronous Machine (PMSM) which weighs 51.6 kg (with brake and gearbox) and has a 91% efficiency at full load (with gearbox) [14]. Since it is a servomotor, it is dynamic enough for the constantly changing operation points. Furthermore, it is lightweight enough to be mounted in a rotating cage, required for launching the kite, so inertia stays low. It is also efficient in motor mode as well as in generator mode. A resolver is fitted to ensure a robust connection over a slip ring. The PMSM is capable of sufficient holding torque (more than 1.8 times the nominal torque), while cooling is not required as the temperature may increase up to 90 °C, limited by the gearbox. A gearbox with ratio 1/3 is included to increase the torque, while the volume of the motor (now with gearbox) stays minimal. The motor is also IP64, so that it can be used outdoors.

The motor is connected via a converter (motor module). This is overdimensioned (45 A nominal current of the motor module vs. 18 A nominal current of the motor) because the motor is capable of overloading (up to 66% in speed and 500% in torque). When accelerating, the current can go up as high as 85 A peak. This motor module is connected via a dc bus to an active front end converter which is connected to the grid via a passive and an active filter. Due to this drive system

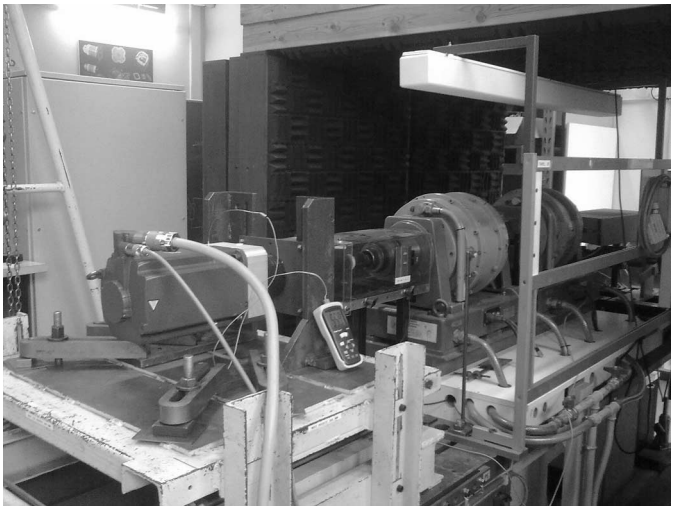


Fig. 4. Motor-mode drive test setup. The motor is connected to the particle and eddy current brake.

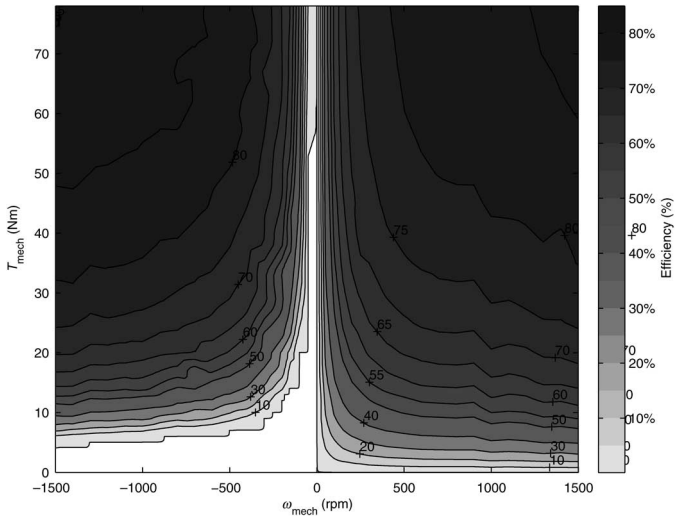


Fig. 5. Measured efficiency map of the drive.

(motor + motor module + active front-end + filters), the operation of the motor is completely decoupled from the grid. Therefore, issues such as low-voltage ride-through and reactive power injection are subject only to the front-end and not to motor operation.

B. Drive Testing

Integrating the drive in the optimization requires some tests in order to parametrize it. The drive properties can easily be derived from the drive datasheet [14]. While the motor is capable of overloading, the nominal motor torque and maximum gearbox speed are chosen as the drive constraint. This is done because the optimal cycles are short (around 6 s) and the drive should not be overloaded too much. Thus, the constraints are 1500 rpm and 78 Nm.

The drive was tested in motor mode and in generator mode. These two modes require different setups, as in the first case, mechanical power needs to be dissipated, and in the second case, mechanical power needs to be supplied to the drive.

1) Motor Mode Setup: The motor is connected to two brakes: a particle brake for low rotational speeds and an eddy current brake for higher rotational speeds. A torque flange is installed between the machine and the brakes in order to read out the mechanical torque. Together with a rotational speed measurement, this torque measurement is used to calculate the mechanical power generated by the drive. The electrical power is measured by connecting a power analyzer to the grid connection of the drive. More than 500 operating points were measured; the rotational speed was varied between 50 and 1500 rpm and the torque was varied between 0 and 78 Nm. These measurements make up the whole motor-operating field. Fig. 4 shows the test setup.

2) Generator Mode Setup: The generator-measuring setup is different from the motor mode-measuring setup since the brakes cannot be used as a motor to drive it. Another drive is thus needed as motor. The measurement setup has an analog torque measuring device which allows to calculate the incoming mechanical power. The generated electrical power is measured by connecting a power analyzer to the grid connection of the drive. More than 500 operating points were measured; the rotational speed was varied between 0 and 3000 rpm and the torque was varied in order to test different generating powers from 0 to 10 kW (power was limited to 10 kW, in order not to overload the machine too excessively). These measurements make up the whole generator-operating field.

3) Measurement Results: The measurements incorporate the efficiencies of all components: gearbox, motor, dc/ac inverter (motor module), and ac/dc converter. As they are dependent on multiple factors, an efficiency map was created which is shown in Fig. 5. With P_{elec} the electrical power, $P_{\mathrm{mech}} = \omega_{\mathrm{mech}} T_{\mathrm{mech}}$ the mechanical power, ω_{mech} the rotational speed, and T_{mech} the torque, the motor efficiency (right-hand side of the map) is calculated as

$$\eta_{\mathrm{mot}} = \frac{P_{\mathrm{mech}}^{\mathrm{output}}}{P_{\mathrm{elec}}^{\mathrm{consumed}}} = \frac{P_{\mathrm{mech}}}{P_{\mathrm{elec}}} \tag{1}$$

while the generator efficiency (left-hand side of the map) is calculated as

$$\eta_{\mathrm{gen}} = \frac{P_{\mathrm{elec}}^{\mathrm{generated}}}{P_{\mathrm{mech}}^{\mathrm{input}}} = \frac{-P_{\mathrm{elec}}}{-P_{\mathrm{mech}}}. \tag{2}$$

Negative efficiencies can occur in generator mode because the drive can consume power ($P_{\mathrm{elec}}^{\mathrm{generated}} < 0$) with positive mechanical input. Another problem occurs on the axes (division by a small number). Because both problems would distort the view, these efficiencies are mapped to zero, which is shown as the white region.

C. Fitting a Parametrized Model

Neither the measurements themselves, nor the efficiency map, can be used directly in the optimization. Instead, a smooth curve is required. This is achieved by reparametrizing a PMSM model [15] and combining this with the data provided by

TABLE I
SOLUTION OF THE LEAST SQUARES PROBLEM

a_0	2.9358×10^2	(W)
a_1	3.5852×10^{-2}	(Nms)
a_2	6.6592×10^{-2}	$((\text{Nms})^{-1})$
a_3	1.0300×10^0	(\)

Siemens in [16]. This yields a drive model including all components, which is a three-dimensional (3-D) curve in function of ω_{mech} and T_{mech}. This model can then be fit to the measured data as a least squares problem.

A PMSM can be modeled as a function of torque, speed, and d-axis current. The d-axis current can again be related to the torque and speed, which is done by the motor controller. Furthermore, friction, related to mechanical power, has to be added to complete the PMSM model [15]. Secondly, the gearbox loss can be related to the mechanical power as well, because this is mostly frictional. Finally, the inverter and converter have to be addressed. From the Siemens catalog [16], it can be derived that the losses in these components are related to the motor current squared and the electrical power plus a constant loss. Since motor current squared equals d-axis current squared plus q-axis current squared, and q-axis current is related to torque [15], also this component is related to torque, speed, and electrical power.

Since all aspects of the drive can be related to rotational speed and torque, one can say that

$$P_{\text{elec}} = f(\omega_{\text{mech}}, T_{\text{mech}}). \tag{3}$$

When calculating with the data provided in [15] and [16], the nonnegligible components in this model would have to be $\omega_{\text{mech}} T_{\text{mech}}$, ω_{mech}^2, and T_{mech}^2 when looking at the drive; a constant term and T_{mech}^2 when looking at the inverter and converter; and $\omega_{\text{mech}} T_{\text{mech}}$ when looking at the gearbox. Therefore, one can say

$$P_{\text{elec}} = a_0 + a_1 \cdot \omega_{\text{mech}}^2 + a_2 \cdot T_{\text{mech}}^2 + a_3 \cdot \omega_{\text{mech}} \cdot T_{\text{mech}}. \tag{4}$$

This fitting problem is a linear least squares problem, the solution is shown in Table I.

Higher order components are obviously present, but of a smaller order of magnitude. This is confirmed when fitting a higher order polynomial on the experimental data. When using a polynomial with terms up to T_{mech}^4 and ω_{mech}^6, the following most important components are $\omega_{\text{mech}}^2 T_{\text{mech}}^2$ and ω_{mech}^4 which are already four orders of magnitude smaller than a_1 and a_2. The proposed curve fit is therefore an accurate fit[1] for the experimental data and an acceptable second-order model for extrapolated cases.

Fig. 6 shows the second-order curve fit, compared with the measured data. For every 500 W, a contour line has been plotted and the zero power lines are thicker. This also shows the accurateness of the fit.

[1]The absolute error is normally distributed with a mean of 0 W and a standard deviation of 1.6% of the nominal power. It is also always smaller than 5% of the nominal power.

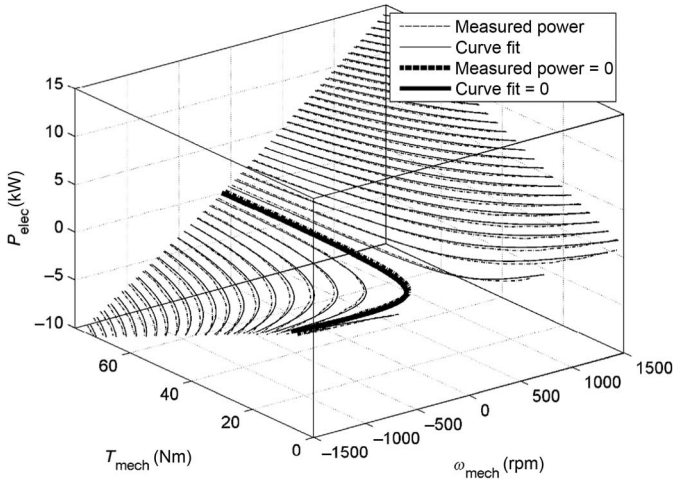


Fig. 6. Power map of the drive, comparing the curve fit with the measured data.

D. Integration in the Optimization

The power map in Fig. 6 visualizes how the drive is implemented in the optimization: a calculation of the electrical power for a specified mechanical torque (T_{mech}) and rotational speed (ω_{mech}) is now possible using a_0, a_1, a_2, and a_3. However, when using this power map to validate electrical power, it is assumed that the measured, steady-state values are a good approximation of the dynamic values. As shown in [17], this approximation is valid and more than 95% accurate.

IV. OPTIMIZATION

The power maximization problem is posed in the form

$$\begin{aligned} \underset{\vec{x}(.),\vec{z}(.),\vec{u}(.),T}{\text{maximize}} \quad & \frac{1}{T}\int_0^T P_{\text{gen}}(\vec{x}(t),\vec{z}(t),\vec{u}(t))\,\mathrm{d}t \\ \text{subject to} \quad & 0 = f(\dot{\vec{x}}(t),\vec{x}(t),\vec{z}(t),\vec{u}(t)), \qquad t \in [0,T] \\ & 0 \geq h(\vec{x}(t),\vec{z}(t),\vec{u}(t)), \qquad t \in [0,T] \\ & T_{\min} \leq T \leq T_{\max} \\ & c(\vec{x}(0),\vec{x}(T)) = 0 \end{aligned} \tag{5}$$

where P_{gen} is the power harvested by the system, either $-P_{\text{elec}}$ or $-P_{\text{mech}}$. The system dynamics are governed by the fully implicit differential algebraic equation f, which describes the 3-D aerodynamic motion of the aircraft. The differential states are $\vec{x} = [\vec{r}, \dot{\vec{r}}, l, \dot{l}, \ddot{l}, R, \vec{\omega}, \vec{\phi}]$, where $\vec{r}$ is the position in Cartesian coordinates $[r_x, r_y, r_z]$, $\vec{\omega}$ is the aircraft angular velocity in the body frame, l is the tether length, R is the direction cosine matrix, and $\vec{\phi}$ are aileron, elevator, and rudder deflections. The control inputs are $\vec{u} = [\dddot{l}, \ddot{\vec{\phi}}]$. The only algebraic variable $\vec{z} = [\lambda]$ is associated with the constraint $r_x^2 + r_y^2 + r_z^2 - l^2 = 0$.

Inequality constraints h include both simple box constraints on states, controls, and ω_{mech} and nonlinear constraints on T_{mech} and aerodynamic angle of attack. Boundary conditions c (given below) enforce both periodicity and consistency of the differential states. The cycle period T is a decision variable in the optimization problem.

The system dynamics, taken from [18], are summarized here. The dynamic equation is

$$\begin{bmatrix} mI_3 & 0 & \vec{r} \\ 0 & J & 0 \\ \vec{r}^T & 0 & 0 \end{bmatrix} \begin{bmatrix} \frac{d}{dt}\dot{\vec{r}} \\ \frac{d}{dt}\vec{\omega} \\ \lambda \end{bmatrix} = \begin{bmatrix} \vec{F}_\mathrm{a}(\vec{x}) - mg\mathbf{1}_z \\ \vec{M}_\mathrm{a}(\vec{x}) - \vec{\omega} \times J\vec{\omega} \\ -\dot{\vec{r}}^T\dot{\vec{r}} + \dot{l}^2 + l\ddot{l} \end{bmatrix} \quad (6)$$

where $\vec{F}_\mathrm{a}$ and $\vec{M}_\mathrm{a}$ are the aerodynamic forces and moments on the kite (detailed in Appendix B), I_3 is the identity matrix, $\mathbf{1}_z = [0, 0, 1]$ is the unit vector in the z-direction, and J is the moment of inertia dyadic of the aircraft. The rotational kinematic equation is

$$\dot{R} = R\,\Omega \quad (7)$$

where Ω is the skew matrix of $\vec{\omega}$. Combining (6) and (7) with the trivial kinematics

$$\frac{\mathrm{d}}{\mathrm{d}t}\begin{bmatrix} \vec{r} \\ l \\ \dot{l} \\ \ddot{l} \\ \vec{\phi} \end{bmatrix} = \begin{bmatrix} \dot{\vec{r}} \\ \dot{l} \\ \ddot{l} \\ \dddot{l} \\ \dot{\vec{\phi}} \end{bmatrix} \quad (8)$$

yields the full model equations f.

Because the model equations use nonminimal coordinates (i.e., there are more generalized coordinates than degrees of freedom), the constraint associated with λ and its derivative must be enforced as initial conditions

$$\begin{aligned} 0 &= r_x(0)^2 + r_y(0)^2 + r_z(0)^2 - l(0)^2 \\ 0 &= r_x(0)\dot{r_x}(0) + r_y(0)\dot{r_y}(0) + r_z(0)\dot{r_z}(0) - l(0)\dot{l}(0). \end{aligned} \quad (9)$$

Likewise, the initial rotation matrix $R(0)$ must be orthonormal. This can be accomplished by enforcing the six upper or lower triangular components of

$$0 = R(0)^T R(0) - I. \quad (10)$$

Because of the nonminimal coordinates, simply enforcing $\vec{x}(0) = \vec{x}(T)$ in order to make the trajectory periodic results in an overconstrained problem. Our periodic conditions are $[l(0), r_y(0), r_z(0), \dot{l}(0), \dot{r_y}(0), \dot{r_z}(0), \ddot{l}(0), \vec{\omega}(0), \vec{\phi}(0)] = [l(T), r_y(T), r_z(T), \dot{l}(T), \dot{r_y}(T), \dot{r_z}(T), \ddot{l}(T), \vec{\omega}(T), \vec{\phi}(T)]$, and the three upper off-diagonal components of $R(0)^T R(T) = I$. These combined with (9) and (10) are the boundary conditions $c(\vec{x}(0), \vec{x}(T))$.

The tether tension is $\lambda\, l$, so the mechanical power P_mech is $-\lambda l\dot{l}$. The drive speed ω_mech and torque T_mech are related to the reel-out speed $\dot{l}$ by the winch radius r_winch

$$\begin{aligned} \omega_\mathrm{mech} &= -\dot{l}/r_\mathrm{winch} \\ T_\mathrm{mech} &= \lambda\, l\, r_\mathrm{winch}. \end{aligned}$$

The electrical power P_elec is then defined by (4).

This optimal control problem (OCP) is solved using the direct collocation technique [19], where a continuous-time OCP is discretized into a nonlinear program (NLP) which is solved with a general-purpose NLP solver. The direct collocation discretization approximates a continuous trajectory with a series of interpolating polynomials whose control points all satisfy the dynamic equation f. See [10] for a more detailed description of the OCP and the direct collocation method.

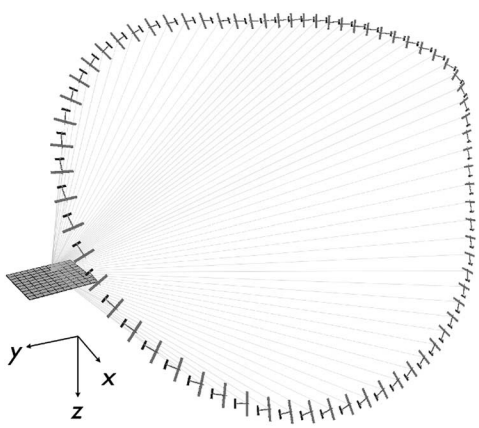


Fig. 7. Typical optimized power-generating trajectory.

We have implemented the direct collocation technique using the CasADi [20] optimization environment, which also provides exact derivatives using algorithmic differentiation. We use IPOPT [21] to solve the NLP. While IPOPT computation times can vary dramatically depending on the initialization, solution times of 30 s are typical on a modern consumer desktop, and negligible overhead is added by the CasADi interface. A typical optimized trajectory is shown in Fig. 7.

V. Results

The optimization was performed for a 7.5 kg, 0.7 m^2 kite for a range of wind conditions. First, the wind speed was varied between 4 and 10 m/s in steps of 1.5 m/s. The average wind speed in Leuven at an altitude of 75 m is 5–5.75 m/s [22], so these give a good range. Second, each optimization was done twice: once for maximal electrical output power and once for maximal mechanical output power. This is most useful as a comparison. Finally, all scenarios are optimized with and without drive constraints. The optimization with drive constraints is the real-world scenario that shows how much energy this system is able to harvest under certain conditions. The optimization without drive constraints is a way of showing what is potentially possible with a larger drive, it thus offers a way to verify the dimensioning.

Each of the scenarios then has a number of outputs that are of interest. The first are the average electrical and mechanical output power. These two numbers combine all the data from one scenario and show the most important part: how much electricity is generated (average electrical power) and how much could have been generated if the conversion was perfect (average mechanical power). All these data are shown in Appendix A and are visualized in Fig. 8. It is important to know that in Fig. 8, in contrast to other figures, the generated power is shown, hence positive power is good and negative power is bad. The second is the torque-speed characteristic. This can be used to visualize each scenario and when plotted together with the

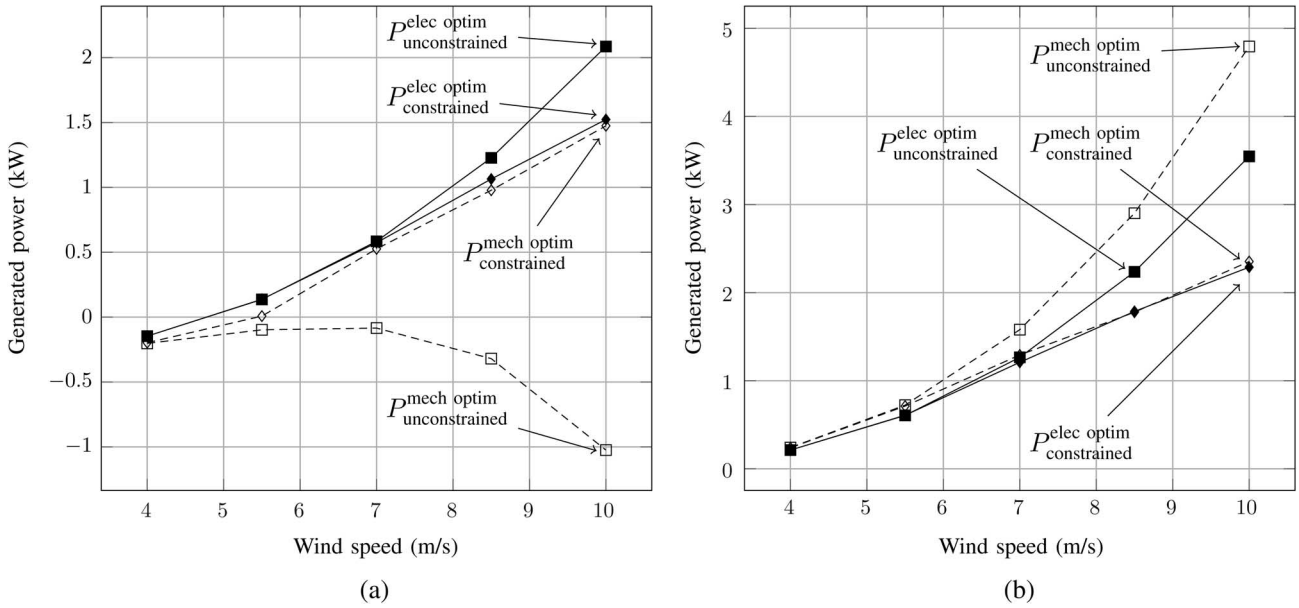


Fig. 8. Optimization results for all scenarios, sorted by electrical (a) and mechanical (b) generated power; sub- and superscripts are used here (and only here) to indicate the scenario, elec/mech optim indicates an electrically or mechanically optimized scenario, (un)constrained indicates an (un)constrained scenario; the data can be found in Table II.

efficiency map, to show how the algorithm uses the efficiency map. A final number of outputs that are useful are the power flows, i.e., the mechanical and electrical power in function of the time. These enable us to look at the instantaneous power and help identify the pumping cycle.

A. Electrical Optimizations

Fig. 8a shows that the electrically optimized results always have a higher electrical power, as should be expected. For the constrained case, the gain is highest at 5.5 m/s, the average wind speed in Leuven. Furthermore, this results in a system that starts generating at lower wind speeds, so the setup could be used more often. When optimizing mechanically, this point lies around 5.5 m/s. However, when optimizing electrically, this point lies around 4.8 m/s.

Fig. 8a also shows the scenarios in which the drive constraints are not used. These results thus show the potential with a bigger drive. It is clear that the difference in electrical powers for this scenario is even bigger. The mechanically optimized cycles only yield negative electrical powers. This is because the operating points have the tendency to go to very high torques at very low speeds. However, this is the most inefficient region for the drive, so it is not generating power at all. When optimizing electrically, the algorithm takes this effect into account and thus electricity is generated. These simulations show the potential for bigger drives. However, they will have different power maps, so forecasting the increase is difficult.

Fig. 9 shows this effect on a torque-speed characteristic of the optimized cycle at 10 m/s (the most extreme case simulated). The time difference between each of the markers is the same, so the densest region in markers is where the kite will operate most of the time. In the zoomed figures, it can be seen that the mechanically optimized scenario (although at much higher torques) is in the least efficient region of the drive. Here, electrical power is either not generated or even consumed. The electrically optimized scenario takes this in account and shifts the operating points to a lower torque, and thus higher efficient, region.

Fig. 10 shows this effect with mechanical and electrical power flows. The mechanically optimized cycles go to much higher powers, where the drive efficiency is very bad. As can be seen in Fig. 10b, the drive consumes almost 10 kW more at its peak. Due to the larger difference between the electrical power and the mechanical power, the mechanically optimized cycle's energy integral is positive, it thus consumes energy. This is definitely not the case for the electrically optimized cycle, since the effect is taken into account, and the cycle requires less peak power and goes to higher efficient regions.

B. Mechanical Optimizations

Fig. 8b shows the average mechanical output powers for all different scenarios. This information could be used to dimension the drive. The mechanically optimized scenarios without constraints show what the maximal output power could be with a perfect drive (100% efficient) and without constraints. This is the same scenario for which Fig. 9 shows the 10 m/s case. As explained above, the densest region is at very high torque and very low speed, thus an inefficient region. The drive could thus be dimensioned for this. However, also a very high speed is required. The maximum speed for this cycle goes up to 3300 rpm. Furthermore, the variety of operating points in a very fast time (a cycle at 10 m/s optimally takes 2.2 s) makes all these demands very challenging to combine into a single drive.

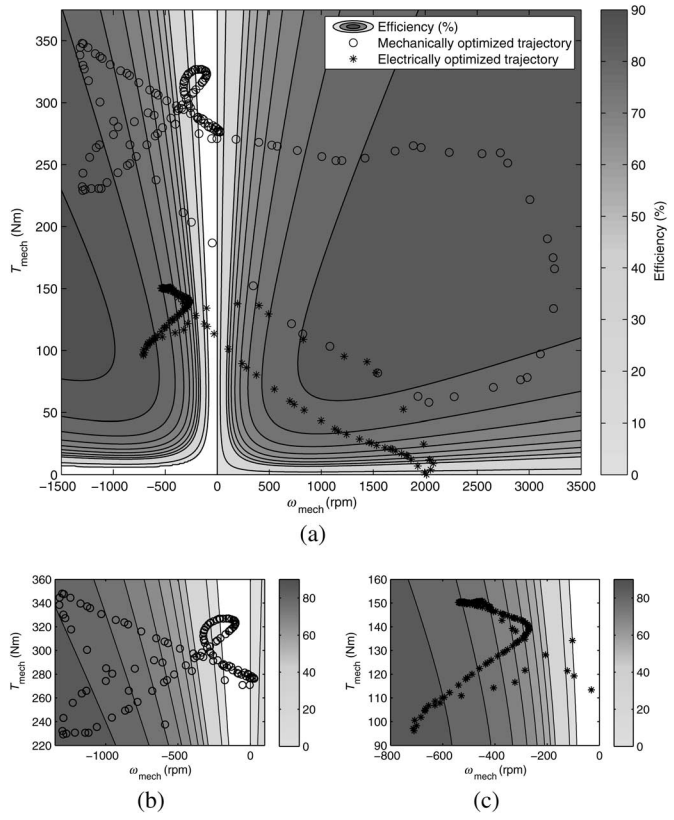


Fig. 9. Torque-speed characteristic at 10 m/s. Comparing between the unconstrained mechanically and electrically optimized scenario, the mechanically unconstrained scenario takes 2.14 s and the electrically unconstrained scenario takes 3.89 s. (a) Both scenarios. (b) Mechanically optimized detail. (c) Electrically optimized detail.

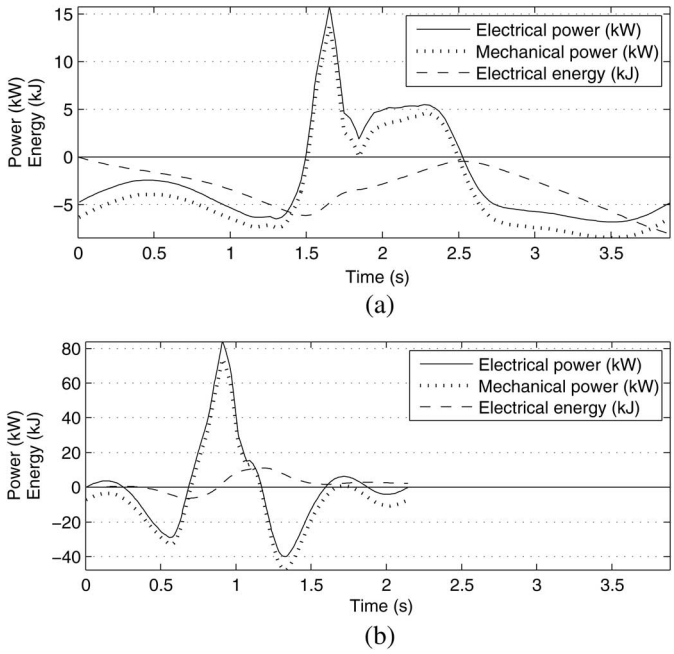


Fig. 10. Comparison in power flows between a mechanically and electrically optimized unconstrained cycle at 10 m/s. (a) Electrically optimized. (b) Mechanically optimized.

C. Impact of Drive Constraints

Fig. 8b also shows something about the effect of the drive and the constraints on the optimal output. The top curve (white squares) shows the optimal scenario. The curve below that (black squares) shows the unconstrained electrically optimized scenario and thus incorporates the effect of the drive efficiency. The two curves below that (diamonds) show the constrained case and thus incorporate the effect of the constraints. The difference between the curves thus shows the effect of the efficiency and the constraints. While the loss due to drive efficiency is omnipresent, the loss due to constraints only shows at higher wind speeds. This is logical as constraints will become active more often at higher wind speeds than at lower wind speeds, and as the wind speed gets higher, this will occur more often. This information thus gives a clue about the relative importance of efficiency and constraints.

The difference between the electrically optimized scenario with constraints (black diamonds) and the mechanically optimized scenario with constraints (white diamonds) becomes smaller at higher wind speeds, as the constraints become more important compared to the drive efficiency.

D. Enabling a Broader Operating Range

Fig. 8a shows all the electrical output powers for all scenarios. It is immediately visible that the mechanically optimized scenarios yield lower powers than the electrically optimized scenarios as was stated above. However, this figure also shows a different important aspect: real-world versus the ideal situation. When comparing the two mechanically optimized systems with each other, it is immediately clear that the difference between the constrained and unconstrained scenario gets bigger and bigger for increasing wind speeds and is only the same around 4 m/s. The same trend can be seen for mechanical power in Fig. 8b, albeit up to 5.5 m/s. This thus means that in case the electrical efficiency is not taken into account (thus mechanically optimized), a bigger drive is immediately required. The effect of the constraints is indeed detrimental.

However, when comparing the electrically optimized constrained and unconstrained scenarios, it is clear that up to 7 m/s, there is no difference between them. Hence, the same drive that could only be used for the 4 m/s scenarios when optimizing mechanically is now capable to work without any losses (due to constraints) up to 7 m/s. Optimizing electrically thus enables a far larger range of wind speeds in which the drive can operate. It thus also results in immediate cost savings due to buying a smaller drive for the same range of wind speeds when compared to a mechanically optimized system.

VI. Conclusion and Outlook

By testing a drive, from grid to outgoing shaft, a power map is created. This can be incorporated, together with drive constraints, in a numerical trajectory optimization. By comparing numerous different scenarios, it is shown that the effect of the electrical conversion, although often ignored due to its high and rather constant efficiency, is very significant. It changes the

TABLE II
AVERAGE ELECTRICAL AND MECHANICAL POWERS FOR ALL SCENARIOS, POSITIVE POWER IS POWER CONSUMED (BAD), NEGATIVE POWER IS POWER GENERATED (GOOD)

			4 m/s	5.5 m/s	7 m/s	8.5 m/s	10 m/s
Constrained	Mechanically optimized	Electrical power (W)	196.99	–7.98	–526.07	–977.95	–1474.25
Constrained	Mechanically optimized	Mechanical power (W)	–238.02	–711.81	–1291.95	–1777.61	–2353.13
Constrained	Electrically optimized	Electrical power (W)	146.45	–137.54	–573.43	–1064.27	–1522.94
Constrained	Electrically optimized	Mechanical power (W)	–212.41	–607.76	–1208.82	–1786.81	–2288.84
Unconstrained	Mechanically optimized	Electrical power (W)	202.11	97.66	84.09	319.78	1024.25
Unconstrained	Mechanically optimized	Mechanical power (W)	–241.06	–722.71	–1579.45	–2901.31	–4794.07
Unconstrained	Electrically optimized	Electrical power (W)	146.45	–136.47	–584.12	–1227.15	–2085.30
Unconstrained	Electrically optimized	Mechanical power (W)	–212.41	–605.64	–1265.41	–2236.33	–3546.30

average electrical output power in low wind speeds considerably and even with high wind speeds, where the operation is limited by drive constraints, the average electrical power can be increased by several percentages. Furthermore, it efficiently enables the use of the same drive in a far broader range of wind speeds and provides more power generated per wing area. The same simulations offer an insight in drive dimensioning as drive efficiency as well as drive constraints have a huge impact on power generation. Therefore, it is worthwhile to include the electrical energy conversion system in future AWE models.

APPENDIX A

Table II shows all the average electrical and mechanical output powers for all scenarios.

APPENDIX B
AERODYNAMIC MODEL

The aerodynamic forces and torques $\vec{F}_\mathrm{a}$, $\vec{M}_\mathrm{a}$ are modeled using a standard force/torque coefficient approach. The aircraft velocity relative to wind $\vec{v}_e$ is given by

$$\vec{v}_e = \dot{\vec{r}} - \vec{w}$$

where $\vec{w}$ is the local static wind. Defining the local unit vector in y direction as $\hat{e}_y = [0, 1, 0]^T$ and the normalized relative wind $\hat{v}_e = \vec{v}_e / \|\vec{v}_e\|$, the forces and moments are given as

$$\vec{F}_\mathrm{a} = \frac{1}{2}\rho \|\vec{v}_e\|^2 S R \left(C_L \vec{e}_y \times \hat{v}_e - C_D \hat{v}_e - C_Y (\vec{e}_y \times \hat{v}_e) \times \hat{v}_e\right)$$
$$\vec{M}_\mathrm{a} = \frac{1}{2}\rho S \|\vec{v}_e\|^2 \left[\, b\, C_l \quad c\, C_m \quad b\, C_n \,\right]^T$$

where ρ is the local air density, S is the reference wing area, b is the reference span, and c is the reference chord. Aerodynamic coefficients of lift C_L, drag C_D, side force C_Y, roll C_l, pitch C_m, and yaw C_n.

Defining the aerodynamic angle of attack α and sideslip angle β as

$$\alpha = \arctan\left(\frac{\vec{v}_{e,z}}{\vec{v}_{e,x}}\right)$$
$$\beta = \arcsin\left(\frac{\vec{v}_{e,y}}{\|\vec{v}_e\|}\right).$$

The moment coefficients are

$$\begin{bmatrix} C_l \\ C_m \\ C_n \end{bmatrix} = \begin{bmatrix} 0 \\ C_{m0} \\ 0 \end{bmatrix} + \begin{bmatrix} C_{l\phi}\, \phi_\mathrm{ail} \\ C_{m\phi}\, \phi_\mathrm{elev} \\ C_{n\phi}\, \phi_\mathrm{rudder} \end{bmatrix} + \begin{bmatrix} C_{lp} & C_{lq} & C_{lr} \\ C_{mp} & C_{mq} & C_{mr} \\ C_{np} & C_{nq} & C_{nr} \end{bmatrix} \begin{bmatrix} b\,\omega_x \\ c\,\omega_y \\ b\,\omega_z \end{bmatrix} \frac{1}{2\|\vec{v}_e\|} + \begin{bmatrix} 0 & C_{l\beta} & C_{l\alpha\beta} \\ C_{m\alpha} & 0 & 0 \\ 0 & C_{n\beta} & C_{n\alpha\beta} \end{bmatrix} \begin{bmatrix} \alpha \\ \beta \\ \alpha\,\beta \end{bmatrix}$$

and the force coefficients are

$$\begin{bmatrix} C_L \\ C_D \\ C_Y \end{bmatrix} = \begin{bmatrix} C_{L0} + C_{L\alpha}\alpha \\ C_{D0} + C_{D\alpha}\alpha + C_{D\alpha 2}\alpha^2 + C_{D\beta 2}\beta^2 \\ C_{Y\beta}\beta \end{bmatrix} + \begin{bmatrix} C_{Le}\, \phi_\mathrm{elev} \\ C_{De}\, \phi_\mathrm{elev} + C_{De2}\, \phi_\mathrm{elev}^2 + C_{D\alpha e}\alpha\, \phi_\mathrm{elev} \\ 0 \end{bmatrix} + \begin{bmatrix} 0 \\ C_{Da}\, \phi_\mathrm{ail} + C_{Da2}\, \phi_\mathrm{ail}^2 + C_{D\beta a}\beta\, \phi_\mathrm{ail} \\ 0 \end{bmatrix} + \begin{bmatrix} 0 \\ C_{Dr2}\, \phi_\mathrm{rudd}^2 + C_{D\beta r}\beta\, \phi_\mathrm{rudd} \\ C_{Yr}\phi_\mathrm{rudd} \end{bmatrix}.$$

REFERENCES

[1] M. Loyd, "Wind driven apparatus for power generation," U.S. Patent 4 251 040, Feb. 17, 1981 [Online]. Available: http://www.google.com/patents/US4251040

[2] K. Geebelen *et al.*, "An experimental test set-up for launch/recovery of an airborne wind energy (AWE) system," in *Proc. Amer. Control Conf.*, 2012, pp. 4405–4410.

[3] M. Clinckemaillie, K. Geebelen, M. Diehl, and D. Vandepitte, "*An experimental set-up for energy generation using balanced kites*," M.S. thesis, Katholieke Univ. Leuven, Leuven, Belgium, 2012.

[4] J. Stuyts and W. Vandermeulen, "*Electrical energy conversion system for pumping airborne wind energy*," M.S. thesis, Katholieke Univ. Leuven, Leuven, Belgium, 2013.

[5] B. Houska and M. Diehl, "Optimal control of towing kites," in *Proc. 45th IEEE Conf. Decision Control*, San Diego, CA, USA, 2006, pp. 2693–2697.

[6] B. Houska and M. Diehl, "Optimal control for power generating kites," in *Proc. 9th Eur. Control Conf.*, Kos, Greece, 2007, pp. 3560–3567 (CD-ROM).

[7] P. Williams, B. Lansdorp, and W. Ockels, "Optimal crosswind towing and power generation with tethered kites," *J. Guid. Control Dyn.*, vol. 31, no. 1, pp. 81–92, Jan./Feb. 2008.
[8] I. Argatov and R. Silvennoinen, "Energy conversion efficiency of the pumping kite wind generator," *Renew. Energy.*, vol. 35, pp. 1052–1060, 2010.
[9] L. Fagiano, M. Milanese, and D. Piga, "Optimization of airborne wind energy generators," *Int. J. Robust Nonlinear Control*, vol. 22, no. 18, pp. 2055–2083, 2012 [Online]. Available: http://dx.doi.org/10.1002/rnc.1808
[10] G. Horn, S. Gros, and M. Diehl, "Numerical trajectory optimization for airborne wind energy systems described by high fidelity aircraft models," in *Airborne Wind Energy*. New York, NY, USA: Springer, 2013, pp. 205–218.
[11] M. S. Ahmed, A. Hably, and S. Bacha, "Kite generator system modeling and grid integration," *IEEE Trans. Sustain. Energy*, vol. 4, no. 4, pp. 968–976, Oct. 2013.
[12] Ampyx Power, *Our Technology* [Online]. Available: http://www.ampyxpower.com/OurTechnology.html, accessed on Oct. 25, 2013.
[13] M. Diehl, "Airborne wind energy: Basic concepts and physical foundations," in *Airborne Wind Energy*. New York, NY, USA: Springer, 2013, pp. 3–22.
[14] Siemens AG, *Catalog D31: SINAMICS and Motors for Single-Axis Drives*, 2012.
[15] S. Morimoto, Y. Tong, Y. Takeda, and T. Hirasa, "Loss minimization control of permanent magnet synchronous motor drives," *IEEE Trans. Ind. Electron.*, vol. 41, no. 5, pp. 511–517, Oct. 1994.
[16] Siemens, *Manual: SINAMICS S120 Booksize Power Units*, 2011.
[17] D. Vanhooydonck *et al.*, "Calculating energy consumption of motor systems with varying load using iso efficiency contours," in *Proc. 19th Int. Conf. Elect. Mach. (ICEM)*, 2010, pp. 1–6.
[18] S. Gros and M. Diehl, "Modeling of airborne wind energy systems in natural coordinates," in *Airborne Wind Energy*. New York, NY, USA: Springer, 2013, pp. 181–203.
[19] L. T. Biegler, "Simultaneous methods for dynamic optimization," in *Nonlinear Programming*. New Delhi, India: SIAM, 2010, pp. 287–324.
[20] J. Andersson, J. Åkesson, and M. Diehl, "CasADi—A symbolic package for automatic differentiation and optimal control," in *Recent Advances in Algorithmic Differentiation*, S. Forth, P. Hovland, E. Phipps, J. Utke, and A. Walther, Eds. Berlin, Germany: Springer-Verlag, 2012.
[21] A. Wächter and L. Biegler, "On the implementation of a primal-dual interior point filter line search algorithm for large-scale nonlinear programming," *Math. Programm.*, vol. 106, no. 1, pp. 25–57, 2006.
[22] Energiesparen, Windsnelheid (m/s) op 75 m ashoogte [Online]. Available: http://www2.vlaanderen.be/economie/energiesparen/img/wind˙kaart.gifl, accessed on Jun. 4, 2013.



Jeroen Stuyts (S'14) was born in Belgium, in 1990. He received the B.Sc. degree in mechanical engineering and M.Sc. degree in energy engineering from KU Leuven, Leuven, Belgium, in 2011 and 2013, respectively. He is currently pursuing the Ph.D. degree at KU Leuven.

His research interests include power electronics, drives, renewable energy sources, and the grid coupling thereof. Currently, he conducts research on high-power grid-friendly converters with fault ride-through capabilities in a distorted low-voltage grid.



Greg Horn was born in the United States, in 1985. He received the B.S. degree in physics from the University of California, Santa Cruz, CA, USA, and the M.S. degree in aeronautics and astronautics from Stanford University, Stanford, CA, USA, in 2009 and 2012, respectively. He is currently pursuing the Ph.D. degree in electrical engineering at KU Leuven, Leuven, Belgium.



Wouter Vandermeulen was born in Belgium, in 1990. He received the B.Sc. and the M.Sc. degrees in energy engineering from KU Leuven, Leuven, Belgium, in 2011 and 2013, respectively.

He is currently working as a Test Engineer with LMS International, a Siemens Business, Leuven, Belgium.



Johan Driesen (S'93–M'97–SM'12) was born in Belgium, in 1973. He received the M.Sc. degree in electrotechnical engineer from KU Leuven, Leuven, Belgium, in 1996. He received the Ph.D. degree in electrical engineering from KU Leuven, in 2000, on the finite element solution of coupled thermal-electromagnetic problems and related applications in electrical machines and drives, microsystems, and power quality issues.

Currently he is a Professor with KU Leuven and teaches power electronics, renewables, and drives. From 2000 to 2001, he was a Visiting Researcher with the Imperial College of Science, Technology and Medicine, London, U.K. In 2002, he was working with the University of California, Berkeley, CA, USA. Currently, he conducts research on distributed energy resources, including renewable energy systems, power electronics and its applications, for instance in renewable energy and electric vehicles.



Moritz Diehl (M'11) was born in Hamburg, Germany, in 1971. He received the Physik-Diplom degrees in physics and mathematics from Heidelberg University and Cambridge University, in 1999, and the Ph.D. degree in scientific computing from Heidelberg University, Heidelberg, Germany in 2001.

From 2006 to 2013, he was a Professor with the Department of Electrical Engineering, KU Leuven University, Leuven, Belgium, and served as the Principal Investigator of the Optimization in Engineering Center (OPTEC), KU Leuven, Leuven, Belgium. His research interests include optimization and control, spanning from numerical methods, and algorithm development to applications in different branches of engineering.

Dr. Diehl holds the Chair of Systems Theory, Control, and Optimization at the Department of Microsystems Engineering, University of Freiburg, Freiburg, Germany, since 2013.